Desalination and Water Treatment
www.deswater.com

doi: 10.5004/dwt.2022.28670

268 (2022) 113–125
August

Boosting hydrogen gas production and mitigation of fluorescein dye on the surface of S-scheme g-C_3N_4/SnO_2 heterojunction

Hisham S.M. Abd-Rabboh[a], A.H. Galal[b,c], Abanoob M. Basely[b], Fatma M. Helmy[b], M.A. Ahmed[b,*]

[a]*Chemistry Department, Faculty of Science, King Khalid University, Abha 61413, Saudi Arabia, email: hsalah@hotmail.com*
[b]*Department of Chemistry, Faculty of Science, Ain Shams University, Abbassia, Cairo 11566, Egypt, Tel. +20 103979568; Fax +20 224831836; emails: abdelhay71@hotmail.com (M.A. Ahmed), Abanoob@yahoo.com (A.M. Basely), Fatma100@hotmail.com (F.M. Helmy)*
[c]*Faculty of Engineering, The British University, Cairo, Egypt, email: hamadagalal2103033@gmail.com*

Received 6 January 2022; Accepted 14 May 2022

ABSTRACT

In this research work, a highly efficient step S-scheme g-C_3N_4/SnO_2 heterojunctions containing various concentration of g-C_3N_4 0–20 wt.% are controllable designed through sonochemical process for generation of hydrogen gas and decomposition of anionic fluorescein dye into eco-friendly species. Spheroid mesoporous SnO_2 nanoparticles were manipulated by controlled sol–gel process. In ultrasonic bath of intensity 150 W, a step S-scheme heterojunctions were constructed by mixing various proportions of g-C_3N_4 and SnO_2 nanoparticles. The change in the physicochemical properties are recorded by high-resolution transmission electron microscopy, X-ray diffraction, N_2 adsorption–desorption isotherm, X-ray photoelectron spectroscopy (XPS), diffuse reflectance spectroscopy and photoluminescence spectroscopy (PL). With introducing 10 wt.% g-C_3N_4, the removal of fluorescein dye reach 92% and hydrogen gas evolution rate is 6.56 mmol/g h which is tenfold higher than that of pristine SnO_2. The shifting in XPS peaks of Sn^{4+} and reduction of PL intensity of the nanocomposite reveal the successful generation of g-C_3N_4/SnO_2 heterojunction. The charge carriers transportation proceeds through step S-scheme mechanism that generate an internal electric fields at the interface boundary between the two semiconductors. The durability of this novel nanocomposite can be deduced from the achievement of 86% of photocatalyst reactivity after six consecutive cycles.

Keywords: Novel g-C_3N_4/SnO_2 nanosheets; Successful dye mitigation; Exceptional hydrogen generation; Massive charge carriers

1. Introduction

The development of low cost and non-toxic photocatalyst is recent challenge for solving energy and environmental problems [1–4]. The generation of hydrogen gas under solar radiations as a zero pollution green energy fuel with strong renewability is hot topics in eliminating the dangerous emissions of fuel resources [5–10]. Among various efficient semiconductors, SnO_2 nanoparticles with unexpected physical and chemical stability has fascinated extensive scientific hotspot field due to its low cost, high surface area, distinct mesoporous structure and strong optical properties compared with well-known metal oxide semiconductors as CeO_2, ZnO and TiO_2. Dilemma, the low charge recombination efficiency and weak redox properties reduces the photocatalytic power of SnO_2 nanoparticles

---

* Corresponding author.

1944-3994/1944-3986

and direct its photocatalytic reactivity to UV region only. Heterojunctions of two appropriate semiconductors displays many benefits over single semiconductor as light harvesting, improving the efficiency of the charge carriers separation and enhancing the oxidative and reductive power of the reactive species. Recently, low-cost g-C_3N_4 is a potential photocatalyst under visible light radiations due to its narrow band gap energy and simple preparation route [11–19]. However, the low surface area, poor efficiency of the charge carriers separation and the low van der Waals interactions among the conjugated planes restrict electron coupling together which reduces the photocatalytic efficiency. Coupling g-C_3N_4 with SnO_2 nanoparticles is recently hot topics for generation of heterojunction with exceptional photocatalytic reactivity [20–25]. Van et al. [20] prepare g-C_3N_4 heterojunction by thermal treatment for $SnCl_4$ and melamine and the results indicate that the novel nanocomposite exhibit a between efficiency in removal of rhodamine B dye. The charge carriers transportation between g-C_3N_4 and promising semiconductors are discussed based on type II heterojunction or charge carriers recombination through direct Z-scheme and step S-scheme [26–33]. Step S-scheme mechanism is most probable pathway for charge carriers transportation that involves the production of internal electric field by recombination of positive hole and negative electrons with low redox potential and preserve the charge carriers with strong redox potential for effective oxidation and reduction processes [34–40]. A few researchers have been concerned on fabricating g-C_3N_4/SnO_2 heterojunction for photocatalytic process [41–48]. The previous researches involve hydrothermal, precipitation, microwave or solid state reaction for construction of g-C_3N_4/SnO_2 heterojunctions. Dilemma, these routes are accompanied with irregular dispersion of the nanoparticles, poor chemical interaction and production of pores constrains that hinders the transportation of reactants molecules. Sonochemistry route is green and low cost operation that generates acoustic cavitation and microjets preventing the particle aggregation and reduces the particle size. The generation of step S-scheme g-C_3N_4/SnO_2 heterojunctions through sonochemical route for photocatalytic purposes is not investigated until now. The selection of the appropriate proportions of g-C_3N_4 in the solid sample is primary key for enhancing the photocatalytic reactivity. The previous research synthesis g-C_3N_4/SnO_2 with high proportion of g-C_3N_4 that reach 50 wt.%. This high proportion of g-C_3N_4 reduces largely the solid surface area, destroy the pore structure and affect the excellent optical properties of SnO_2. In our research, we select an appropriate amount of g-C_3N_4 (10 wt.%) that enhances the photocatalytic properties of SnO_2 without affecting its physicochemical properties. The as-synthesized heterojunctions were analyzed by X-ray photoelectron spectroscopy (XPS), X-ray diffraction, high-resolution transmission electron microscopy (HRTEM), diffuse reflectance spectroscopy (DRS), photoluminescence spectroscopy (PL) and Brunauer–Emmett–Teller (BET). The photocatalytic performance of the bare and the hybrid nanocomposites was explored by following the decomposition of fluorescein dye degradation and the photocatalytic hydrogen production as clean renewable energy. The mechanism of charge transportation is investigated and deliberated using trapping scavenger experiments and PL studied of terephthalic acid.

2. Material

Isopropanol terephthalic acid, ammonium oxalate, ammonia solution, urea, absolute ethanol, stannic chloride pentahydrate, ammonia solution, methanol, fluorescein dye and benzoquinone were collected from Sigma-Aldrich Company with purity = 99%.

2.1. Synthesis of g-C_3N_4 nanoparticles

2.1.1. Synthesis of g-C_3N_4 nanoparticles

Typically, 35 g of microcrystalline urea were calcined at 560°C with rate 2°C/min and left for 7 h in covered aluminum crucible. The calcined solid after cooling to 30°C was purify with ethanol (99%) and grinding with solid mortar. The final generated g-C_3N_4 nanosheets are characterized with their brilliant brownish yellow color assigned to successful route for synthesis of g-C_3N_4.

2.1.2. Preparation of SnO_2 nanoparticles

SnO_2 nanoparticles are usually well synthesized by controlled sol–gel technology [48,49]. Typically, 3 g of pluronic template dissolved in 100 mL ethylene glycol added to a solution containing 17 g $SnCl_4{\cdot}5H_2O$ dissolved in 120 mL ethylene glycol. Afterwhile, the mixture was subjected to constant stirring for 12 h. Ammonia solution of concentration 2 M was added dropwise to the above mixture with constant stirring until the pH of solution is maintained at pH = 9. Then, the sol was left for another 5 h with constant stirring. Finally, ultrasonic bath with intensity 150 W was applied to sol mixture for 1 h. The colloidal mixture was left for 10 h followed by filtration and washed with bi-distilled water to mitigate chloride ions. Then, the gel mixture was dried at 90°C for 24 h. The dried solid was calcined at 450°C with rate 2°C/min for 5 h.

2.1.3. Preparation of g-C_3N_4/SnO_2 heterojunctions

In high performance ultrasonic bath with 150 W intensity, a calculated amount of g-C_3N_4 nanosheets and SnO_2 nanoparticles are mixed together in distilled water by different proportions to generate heterojunctions with 5, 10, 15 and 20 w/w% g-C_3N_4 decorating pristine tin oxide. The pristine specimens are denoted as g-$C_3N_4$and SnO_2 and the heterojunctions denoted as SnCN5, SnCN10, SnCN15 and SnCN20 referred to the hybrid nanoparticles containing 5, 10, 15 and 20 wt.% of g-C_3N_4 contents.

2.2. Material characterization

The heterojunction crystalline phases were explored by P'Analytical X'PERT MPD diffractometer purchased from the United States. The pore structure and surface area analysis were recorded by adsorption isotherms of N_2 gas. XPS analysis for estimation of oxidation state and elemental compositions was carried out by K-ALPHA Themo Fisher Scientific, USA technique with monochromatic X-ray

Al K*α* radiation from 10 to 1,350 eV. Transmission electron microscope with high resolution were detected by HRTEM JEOL 6340. The reflectance and the band gap energy of the solid specimens were recorded by JASCO spectrometer (V-570) from United States. The mitigation of anionic fluorescein dye under 300 W intensity solar simulator is taken as photocatalytic reaction model to elaborate the removal tendency of the as-synthesized heterojunction. Typically, 100 mL of the anionic dye was mixed with 0.1 g of the photocatalyst with constant stirring for 1 h to reach adsorption–desorption equilibrium that depend on the affinity of the solid surface to attract the dye molecules through adsorption process. Afterwhile, the mixture was irradiated with xenon lamp of 300 W intensity for 2 h to investigate the photocatalytic kinetic rate. At each interval time, 3 mL of the solution is separated, centrifuged and the color intensity is recorded by UV-Visible spectrophotometer. The generation of 2-hydroxy terephthalic acid is taken as indicator for concentration of Hydroxyl radicals. The concentration of H_2 gas evolved under 300 W Xenon lamp as light source was recorded by dispersing various specimens of the heterojunctions into 180 mL of methanol solution. 600 µL gaseous products were taken and analyzed by gas chromatography for various interval times of hydrogen production process.

3. Results and discussion

3.1. Physicochemical characterization

The diffraction pattern of the as-synthesized photocatalysts are recorded in Fig. 1a. The well-known crystalline peaks at 2θ = 26.7°, 34.4°, 37.5°, 51.7°, 54.9°, 58.4°, 61.8° and 65.1° are referred to SnO_2 tetragonal structure. On the other hand, the prevailing diffraction peaks produced at 13.2° and 27.59° are related to (100) and (002) diffraction planes, respectively which are consistent to $g\text{-}C_3N_4$ (JCPDS no. 87–1526). The main characteristics diffraction peaks of $g\text{-}C_3N_4$ are emerged in the nanocomposites under the strong

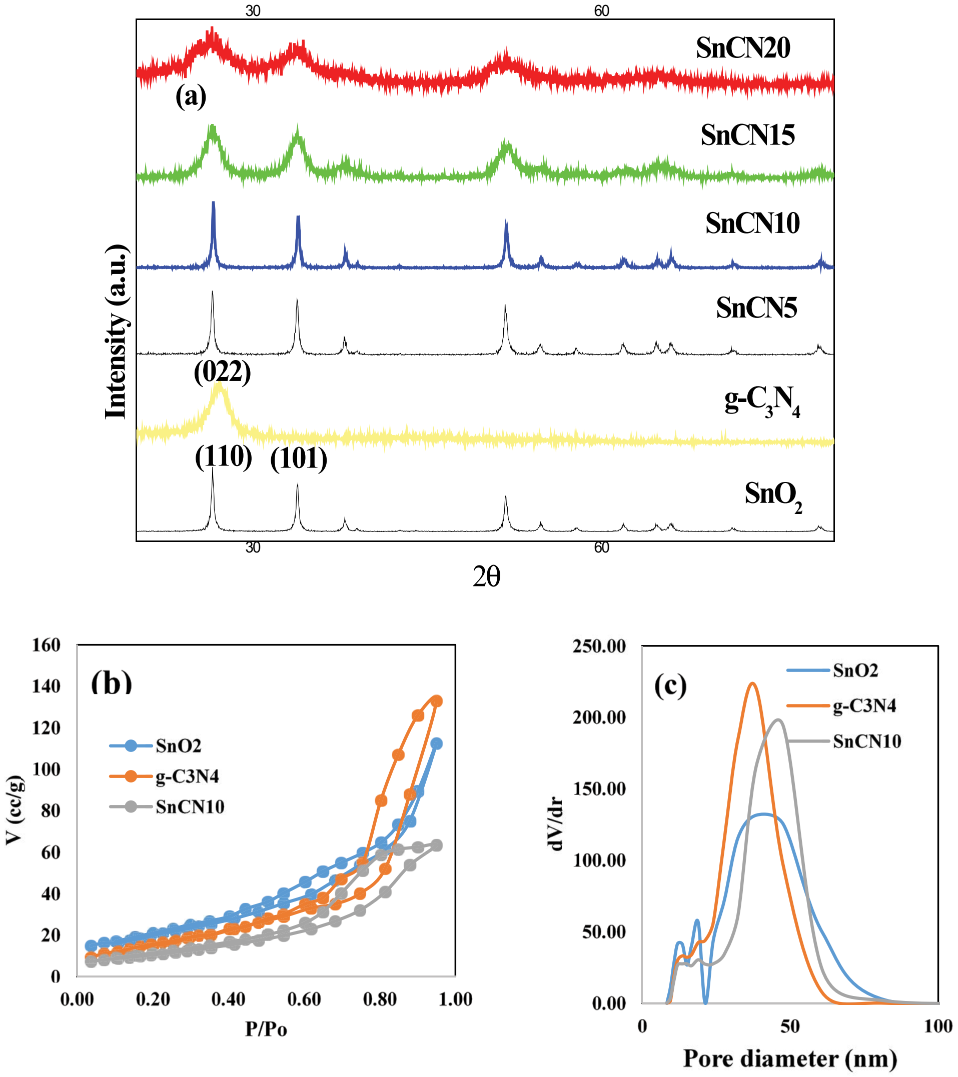

Fig. 1. (a) X-ray diffraction of SnO_2, $g\text{-}C_3N_4$, SnCN5, SnCN10, SnCN15 and SnCN20, (b) N_2 adsorption–desorption isotherm of SnO_2, $g\text{-}C_3N_4$ and SnCN10, and (c) pore size distribution curve of SnO_2, $g\text{-}C_3N_4$ and SnCN10.

crystalline peaks of SnO_2, however, the two peaks for the sample SnCN20 are very broad that embedded the diffraction peaks of both SnO_2 and g-C_3N_4, this phenomenon is in agreement with previous results of Wu et al. [47] and Van et al. [20] who report that the crystalline peaks of g-C_3N_4 commence to appear when the concentration of g-C_3N_4 to SnO_2 is 1:1 by wt.%. The crystalline dimensions estimated by Debye–Scherrer equation is 49, 54, 36, 28, 22 and 15 nm for SnO_2, g-C_3N_4, SnCN5, SnCN10, SnCN15 and SnCN20, respectively. Among incorporation of g-C_3N_4, the crystalline dimensions are strongly depressed due to diffusion of g-C_3N_4 nanosheets between SnO_2 nanoparticles. The adsorption–desorption isotherms of nitrogen at 77 K on pristine SnO_2, g-C_3N_4 and SnCN10 heterojunction (Fig. 1b) are classified as Type IV adsorption–desorption isotherms according to IUPAC classifications with H1 hysteresis loop. H1 hysteresis loop referred to open porous matrix that explains the construction of definite mesoporous heterojunctions with cylindrical pore structure. This cylindrical pore structure is recommended to facilitate the transportation of reactants molecules without existence of any pore restrictions that increases the rate of the photocatalytic processes. The surface area of SnO_2, g-C_3N_4 and SnCN10 nanoparticles calculated from BET equation in its normal range of applicability are 103, 78 and 67 m^2/g. The BJH pore size distribution curve is constructed on SnO_2, g-C_3N_4 and SnCN10 nanoparticles indicating that the pore diameter is 38.4, 46.5 and 38.8 nm revealing the predominant mesoporous structure of the pristine and the nanocomposite solid sample.

Sample	Particle size (nm)	Surface area (m^2/g)	Pore diameter (nm)	Band gap energy (eV)
SnO_2	49	103	38.2	3.15
g-C_3N_4	54	78	45.6	2.58
SnCN10	28	67	38.8	2.79

The elemental composition of SnO_2 (Fig. 2a and b) and g-C_3N_4/SnO_2 heterojunction containing 10 wt.% g-C_3N_4 (Fig. 2c–f) was elaborated by XPS analysis that records the high purity of the as-synthesized nanocomposites. The asymmetric O 1s with binding energy 531.28 eV in SnO_2 and 530.8 eV in the nanocomposites is assigned to oxygen species. The Sn 3d spectrum illustrates a broad peaks at binding energies of 487.1 and 495.1 eV, referred to Sn $3d_{5/2}$ and Sn $3d_{3/2}$ oxidation states, respectively. These two bands are shifted to 487.5 and 495.6 in the nanocomposite specimens. This shift in the value of binding energy to high value supports the strong chemical interactions between g-C_3N_4 and SnO_2 and formation of successful heterojunction. The orbit splitting separation between the two peaks is 7.8 eV revealing Sn^{4+} production. The existence of C 1s is elaborated by production of two peaks at 284.85 and 287.22 eV assigned to C–C and C–N or C–$(N)_3$ group of g-C_3N_4, respectively. The two peaks at 398.47 eV and 404.12 eV are referred to (C–N–C) and N–$(C)_3$, respectively. The spheroid structure of SnO_2 and the spongy structure of g-C_3N_4 are well discovered by field-emission scanning electron microscopy (Fig. 3a and b), respectively. It is worth-noting to observe the dispersion of SnO_2 nanoparticles on g-C_3N_4 sheets for the sample SnCN10 (Fig. 3c). HRTEM for SnO_2, g-C_3N_4 and SnCN10 are recorded in Fig. 3d–f. Fig. 3d illustrates the tetragonal structure of SnO_2 with perfect crystallization. However, Fig. 3e represents the sheet structure of graphitic carbon nitride. The distribution of tetragonal SnO_2 on g-C_3N_4 sheets is recorded in Fig. 3f that reveal the successful heterojunction generation between SnO_2 and g-C_3N_4 sheets. The crystallinity and the heterojunction generation is further elaborated by SAED analysis (Fig. 3g–i). The diffraction rings recorded at (100) and (002) planes are belongs to g-C_3N_4 crystalline planes. On the other hand, the diffraction rings at (110), (101), (200) and (211) are ascribed to SnO_2 tetragonal crystalline planes. On careful examining Fig. 3i, one can observe the existence of different rings belong to g-C_3N_4 and SnO_2 revealing the successful generation of step-S scheme heterojunction. DRS analysis examines the optical properties and the strong absorbability of the solid specimens in the visible region. Fig. 4a displays an absorption band edge at 405 nm referred to SnO_2 intrinsic absorption of SnO_2 and other one at 485 referred to the absorbability of g-C_3N_4 nanosheets in the visible region (Fig. 4a). 3.15, 2.58 and 2.79 are the band gap energy calculated based on Tauc equation for SnO_2, g-C_3N_4 and SnCN10, respectively (Fig. 4b). The conduction and valence band potentials are1.19 and +1.39 eV for g-C_3N_4 and +0.125 and +3.275 eV for SnO_2, respectively. The separation efficiency of the massive charge carrier is elaborated from PL analysis of solid specimens. The remarkable signal at 438 nm assigned to charge transportation between valence and conduction bands. This signal is depressed in the heterojunction compared with pristine sample is attributed to the better charge carriers separation efficiency on coupling SnO_2 with g-C_3N_4.

3.2. Photocatalytic degradation of fluorescein dye

Fluorescein (FLU) dye is exploited in the industry of textile fabric and cosmetics, which produce serious problems on human and animal skins and affected the eco-system. The removal of this toxic dye that spoiled the environmental system is required for environmental purposes. fluorescein dye was selected as primary anionic pollutant model due to the point of zero charge of the nanocomposite measured by zeta potential is (PZC, pH = 6.8) which make surface is very acceptable for anionic dye. Fluorescein dye is extensively used in cosmetics, textile industry and manufacture of food sweets possesses high stability due to the aromatic structure that persist the degradation by biological species. A few research was carried out to examine the photodegradation of this anionic dye under visible light radiations.

The photocatalytic efficiency of the as-synthesized heterojunction was inquired by following the decomposition of fluorescein dye as anionic pollutant model. A weak photocatalytic reactivity in the visible light of pristine SnO_2 and g-C_3N_4 was attributed to the low efficiency of massive charge carriers separation. All the as-synthesized samples record high decomposition rate influenced by the concentration of g-C_3N_4 in the nanocomposites (Fig. 5a). Nanocomposites containing 10 wt.% g-C_3N_4.record the optimum reactivity that decompose 92% of fluorescein dye compared with 45% decomposition on pristine SnO_2. The catalytic

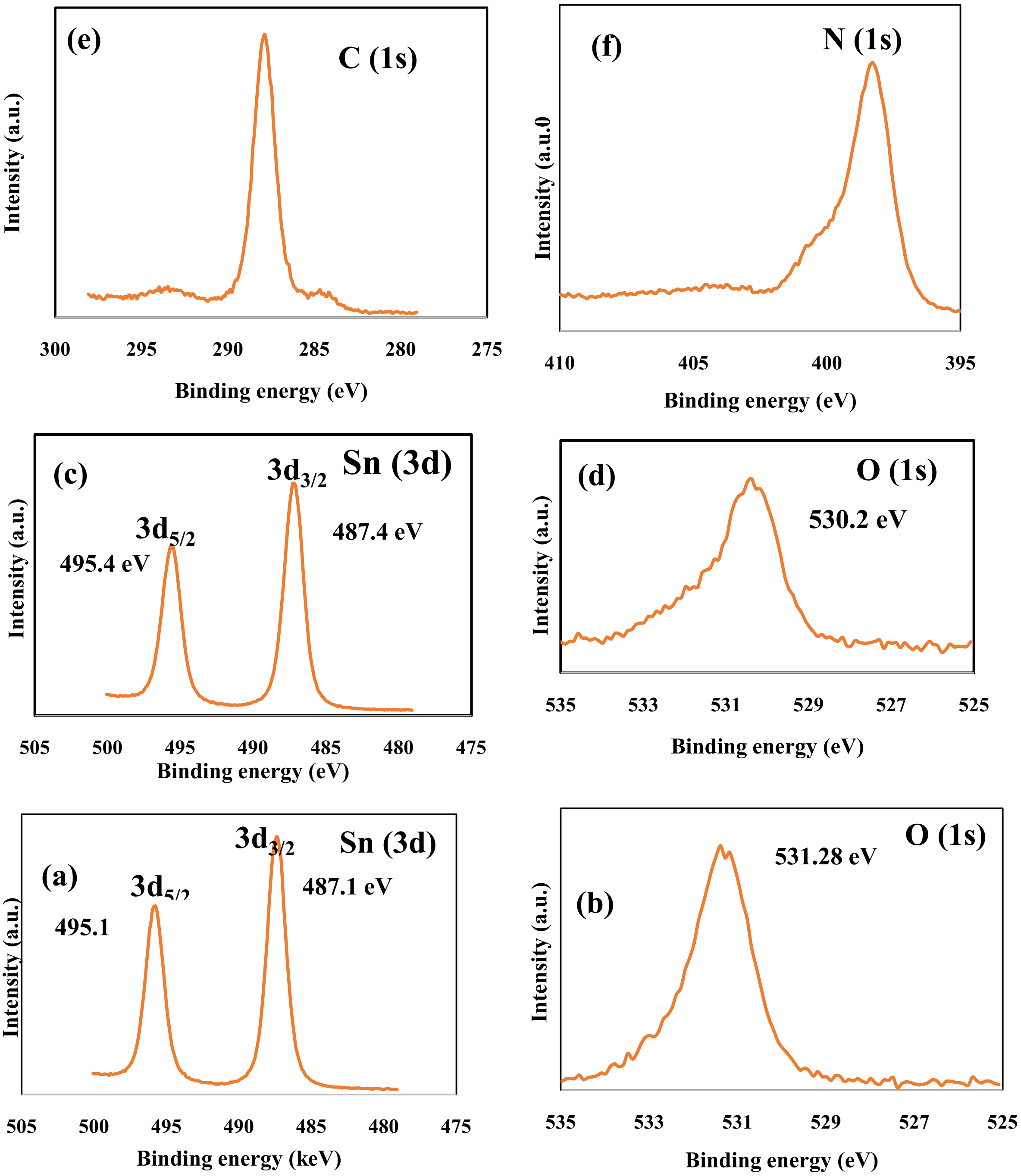

Fig. 2. XPS of (a) Sn and (b) O in SnO_2 and (c) Sn, (d) O, (e) C, and (f) N in SnCN10.

decomposition rate depress upon increasing the concentration of g-C_3N_4 due to the accumulation of g-C_3N_4 nanosheets that inhibit the transportation of charge carriers to dye solution. The photocatalytic dye decomposition follow the pseudo-first-order equation with rate constant 0.0023, 0.0065, 0.0035, 0.0067, 0.026 and 0.0036 for SnO_2, g-C_3N_4, SnCN5, SnCN10, SnCN15 and SnCN20, respectively (Fig. 5b). The production of 2-hydroxy terephthalic acid (Fig. 5c) suggest the generation of hydroxyl groups with concentration being increases with time of visible light exposure for the sample SnCN10. The trapping experiments are carried out to explore the primary species responsible for dye decomposition using isopropanol, $AgNO_3$, ammonium oxalate and benzoquinone for capture hydroxyl radicals, electron conduction band, positive hole and superoxide radicals, respectively (Fig. 5d). With introducing isopropanol, ammonium oxalate and benzoquinone, the rate of dye decomposition is greatly reduced. $AgNO_3$ show a negligible effect in dye

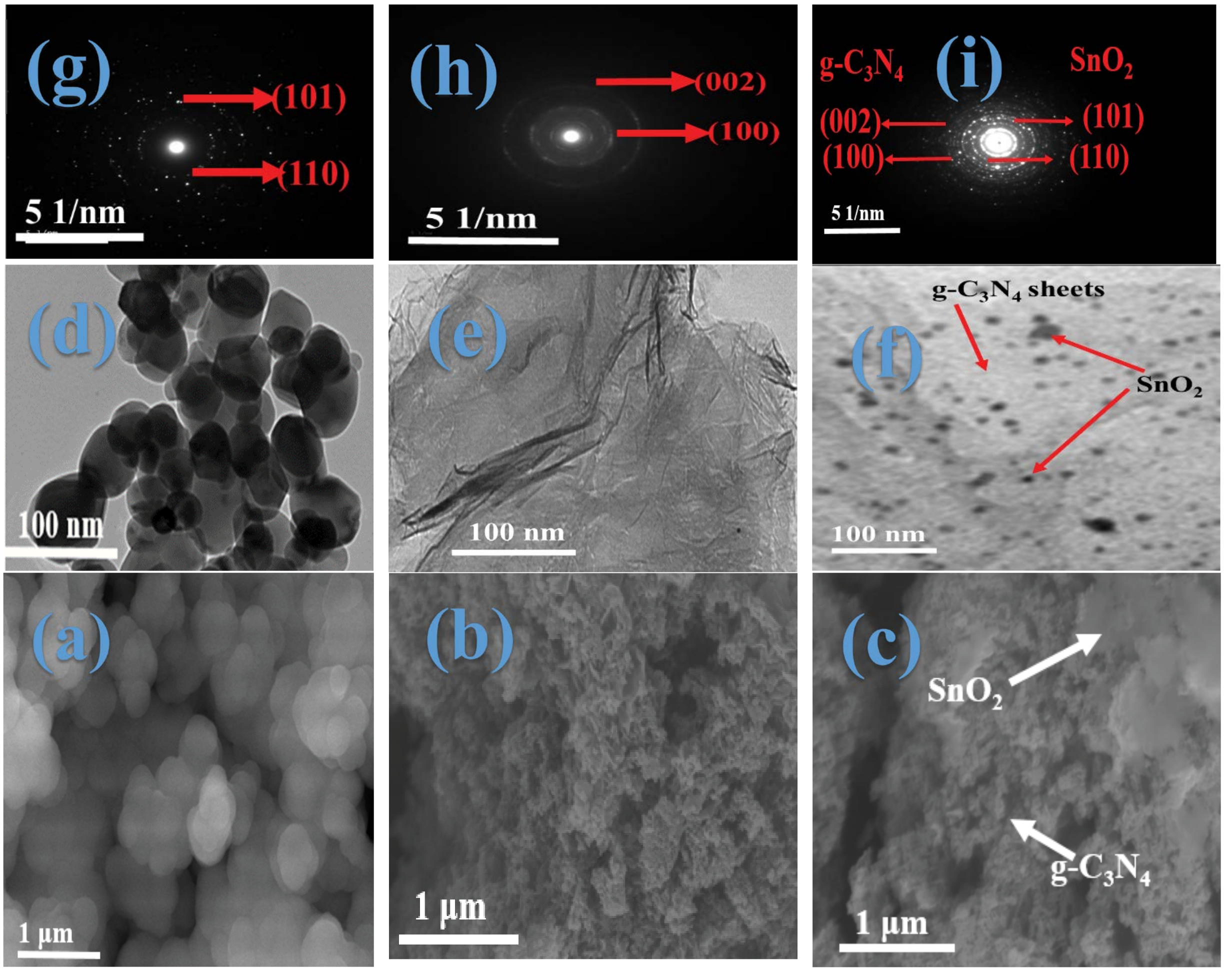

Fig. 3. Field-emission scanning electron microscopy of (a) SnO_2, (b) $g-C_3N_4$ and (c) SnCN10, HRTEM of (d) SnO_2, (e) $g-C_3N_4$ and (f) SnCN10 and SAED of (g) SnO_2, (h) $g-C_3N_4$, and (i) SnCN10.

degradation revealing the small effect of electron conduction band in dye degradation. The experimental work have pointed out that the maximum photocatalytic efficiency is recorded for 0.1 g of the photocatalyst followed by a depression in the degradation process due to the pronounced turbidity of the dye solution upon increasing the weight of catalyst (Fig. 5e). These turbidity reduces the light penetration on the photocatalyst surface and decreases the number of radicals produced. The influenced of pH of the solution on the photocatalytic process is illustrated in Fig. 5f that indicate that the maximum reactivity is observed at pH = 6 near the isoelectric point of SnCN10 (PZC, pH = 5.8). At low pH, the interaction between H^+ and the anionic dye decreases the degradation due to adsorption of large amount of dye on the photocatalyst surface. The adsorption of large number of dye molecules block the active centers and prevent the production of charge carriers and reactive radicals. At high pH, the repulsion between the anionic dye and OH^- of the solution reduces the chance for dye distribution near the solid surface to be decomposed by the charge carriers. The influence of initial dye concentration ($1 \times 10^{-5} – 5 \times 10^{-5}$) on the photocatalytic degradation removal was carried under the same reaction conditions (Fig. 5g). The experimental results indicate the high efficiency of the optimum photocatalyst SnCN10 on removal of 96% of the dye under the various dye concentration. SnCN10 heterojunction displays the same decomposition rate after six consecutive cycles revealing the high stability of the nanocomposite to be involved on industrial scale (Fig. 5h).

Total organic carbon (TOC) analysis was carried out to confirm the degradation of fluorescein dye into eco-friendly species as CO_2 and H_2O. The experimental results proved that TOC depress from 45.3 to 5.8 mg/L confirm the complete dye degradation

3.3. Photocatalytic hydrogen production

The photocatalytic hydrogen production was elaborated on the as-synthesized heterojunctions containing various proportions of $g-C_3N_4$ with methanol as hole trapping species (Fig. 6a). The fast recombination of the massive charge carriers in $g-C_3N_4$ accounts for its weak photocatalytic reactivity. The hydrogen gas concentration generated on $g-C_3N_4$ surface is 0.79 mmol/h g after 2 h of the reaction. The photocatalytic hydrogen evolution rate enhances rapidly with increasing $g-C_3N_4$ compositions and reach 6.77 $mmolg^{-1}h^{-1}$

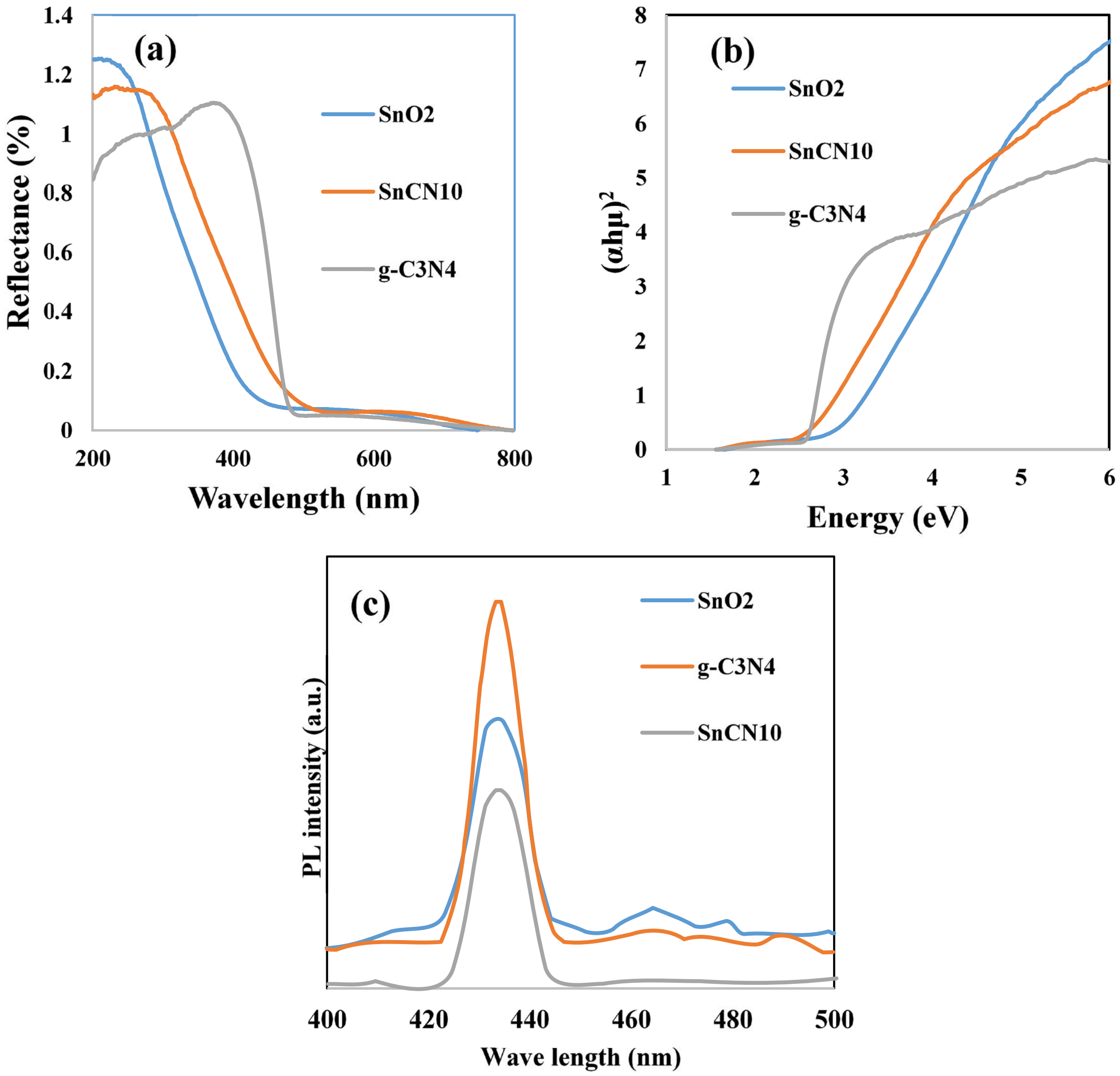

Fig. 4. (a) DRS of SnO_2 and g-C_3N_4, (b) Tauc plot of SnO_2 and g-C_3N_4 and (c) PL of SnO_2 and g-C_3N_4 and SnCN10.

for SnCN10 heterojunction. The primary role of g-C_3N_4 is concerned with promoting the charge carrier separation efficiency and shifting the specimen reactivity to visible region. The successive deposition of g-C_3N_4 layers on SnO_2 nanoparticles inhibit the migration of positive holes to the solution mixture and act as novel recombination centers. The effect of catalyst weight on the photocatalytic hydrogen production for the heterojunction SnCN10 is recorded in Fig. 6b. The photocatalytic reactivity enhances rapidly with increasing weight of photocatalyst up to 1 g/L. Further, increasing in photocatalyst weight turns the solution too cloudy to facilitate the light penetration. The amount of hydrogen gas is sensitive to pH of mixture solution. The amount of hydrogen gas generated on SnCN10 approach a maximum at pH = 7 (Fig. 6c). At pH value lower than 7, methanol protonation is proceed decreasing the concentration of hydrogen gas evolved. On the other hand, at pH higher than 7, a remarkable reduction in H^+ concentration affect the generation of hydrogen gas. The durability of SnCN10 photocatalyst is tested by recycling the production of hydrogen for six consecutive cycles. Fig. 6d records the durability of SnCN10 for six consecutive cycles in generating nearly the same concentration of hydrogen gas evolve.

3.4. The mechanism of charge carrier transportation

The mechanism of the massive charge carriers transportation along the interfacial surface between two semiconductors was recorded by different aspects. The electron transportation from more to less conduction band potential and the migration of the positive holes from more to less valence band potential are ascribed to traditional type (II) heterojunction. The removal of the massive charge carriers with low redox potential and the preservation of the charge carriers with high redox potential are attributed to Z-scheme route. Recently, step S-scheme mechanism is more promising in analyzing the charge carrier migration along the interfacial surface between two semiconductors.

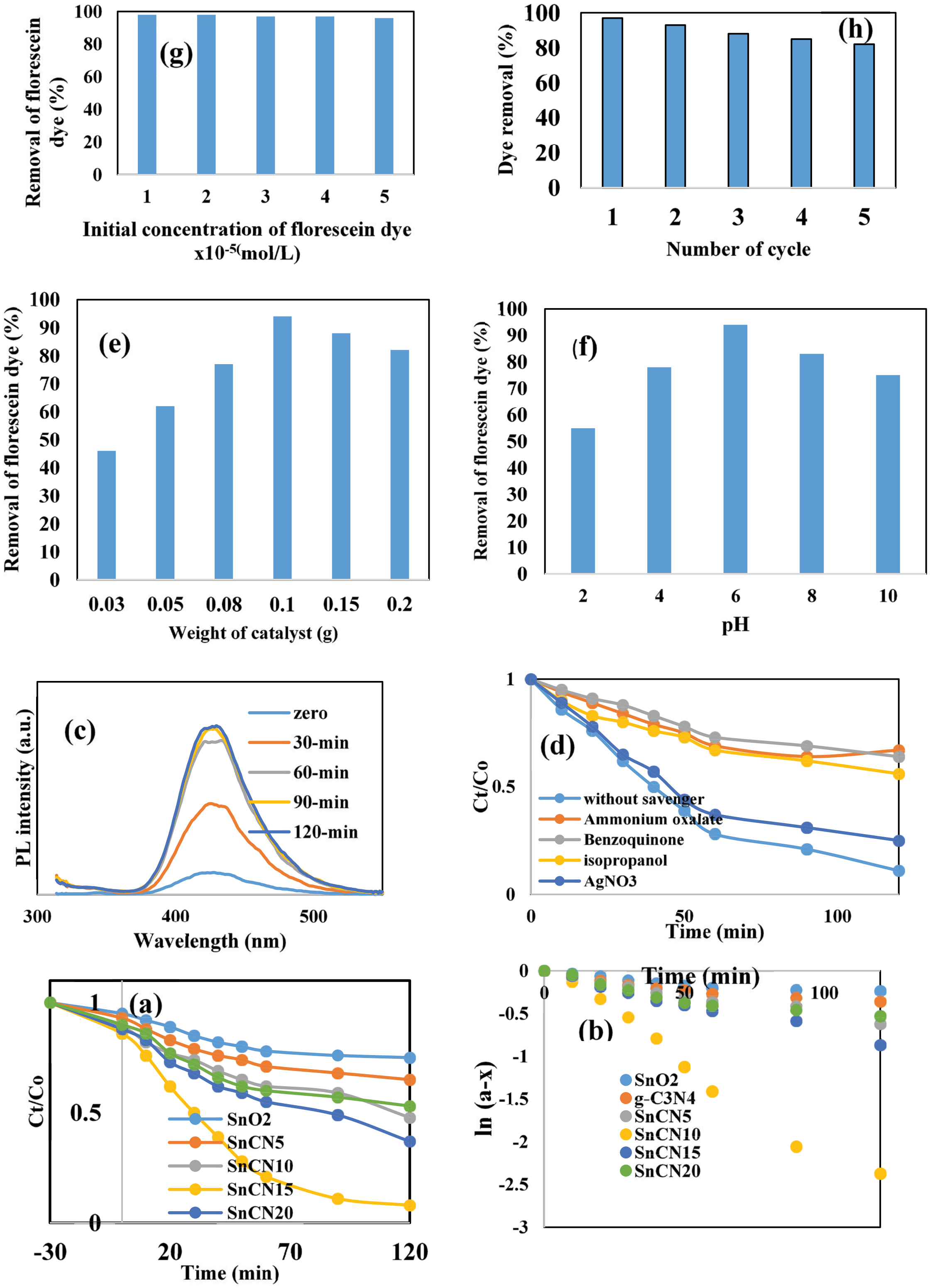

Fig. 5. (a) Variation of photodegradation of fluorescein dye over SnO_2, g-C_3N_4, SnCN5, SnCN10, SnCN15 and SnCN20 with time of irradiations, (b) pseudo-first-order plot for photocatalytic degradation of fluorescein dye over SnO_2, g-C_3N_4, SnCN5, SnCN10, SnCN15 and SnCN20, (c) PL of terephthalic acid over SnCN10, (d) effect of various scavengers over SnCN10, (e) effect of catalyst weight on the photocatalytic removal of fluorescein dye (%), (f) effect of pH on the photocatalytic removal of fluorescein dye (%), (g) effect of initial concentration of dye on photocatalytic removal of fluorescein dye (%) and (h) regeneration of SnCN10 for six consecutive cycles.

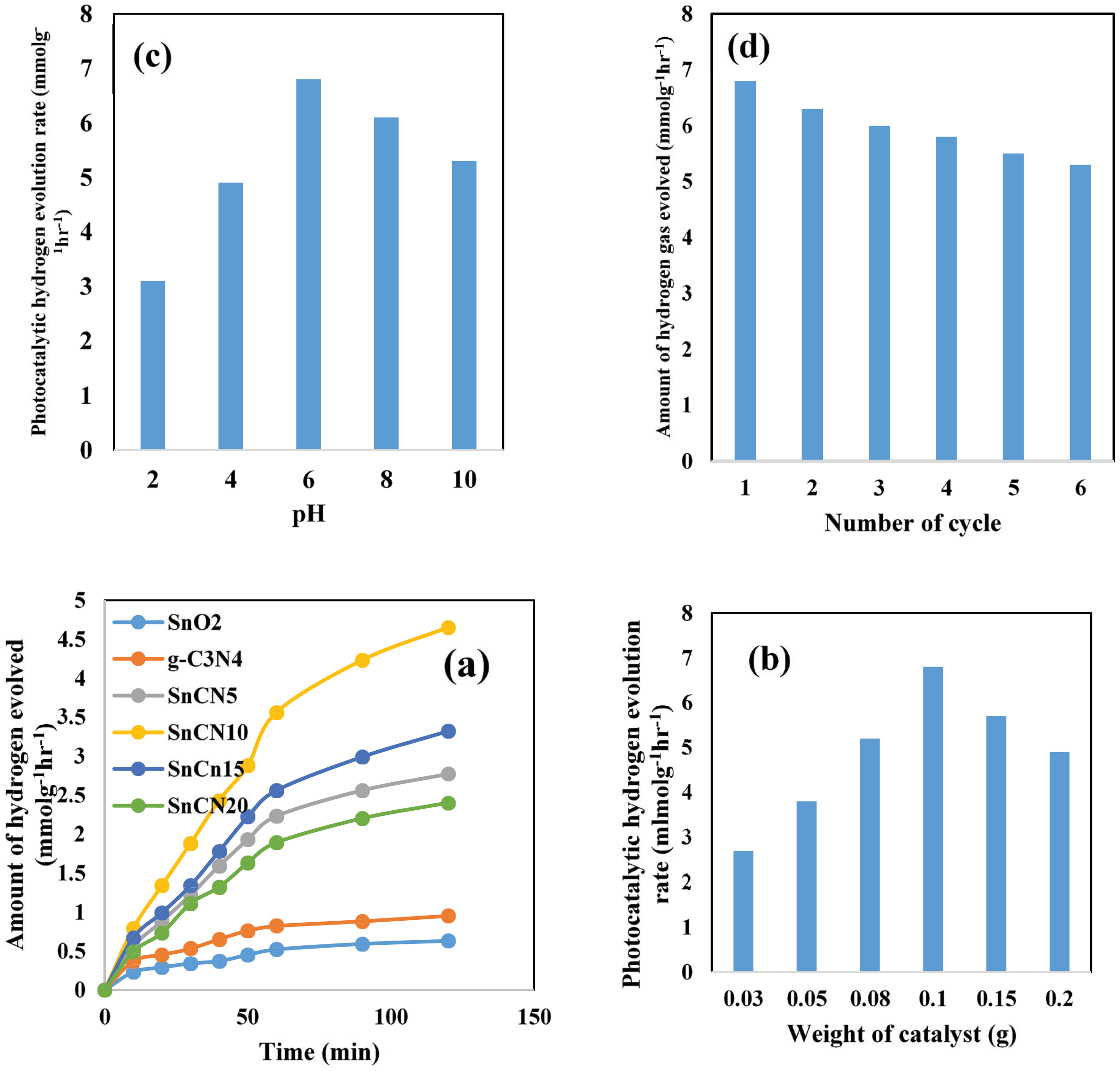

Fig. 6. (a) The influence of amount of g-C_3N_4 on the amount of hydrogen evolved (mmol/g h), (b) effect of catalyst weight on the photocatalytic hydrogen evolution rate (mmol/g h), (c) effect of pH on the photocatalytic hydrogen evolution rate (mmol/g h), and (d) regeneration of SnCN10 for six consecutive cycles.

The electron transportation is more like "Step" that generate an internal electric field due to diffusion of electrons of the reductive photocatalyst to oxidative photocatalyst with formation of electron depletion and accumulation layers. As results of this electron transportation, a negative charge is created on the oxidative photocatalyst and a positive charge is generated on reductive photocatalyst producing internal electric field motion flows from reductive to oxidative photocatalyst which is accompanied by migration of the photogenerated electrons transfer from oxidative to reductive photocatalyst. As a result for this phenomenon, the Fermi level of the oxidative and reductive photocatalyst are aligned to the same level due to direct contact between the two semiconductors through upward and downward shift in the Fermi levels of oxidative and reductive photocatalyst, respectively. At the last stage, the photogenerated massive charge carriers of lower oxidative and reductive potentials are recombined through electrostatic attraction force. However, the charge carriers with high redox properties are maintained with strong redox power for photocatalytic processes. The charge transportation suggested by S-scheme g-C_3N_4/SnO_2 hybrid photocatalyst is demonstrated in Fig. 7 which indicate the existence of two active visible light absorption centers, being SnO_2 nanoparticles and g-C_3N_4 nanosheets. The electron transportation from g-C_3N_4 to SnO_2 conduction band and the holes transfer from SnO_2 to g-C_3N_4 valence band as assumed by type (II) heterojunction features cannot account for generation of hydroxyl radicals with potential of $OH^-/OH^\bullet$ = 2.88 eV. Moreover, the conduction band of SnO_2 is +0.125 eV cannot allowed the production of hydrogen gas [$E_{H+/H2}$ = zero]. On the light of step S-scheme mechanism, g-C_3N_4 positive

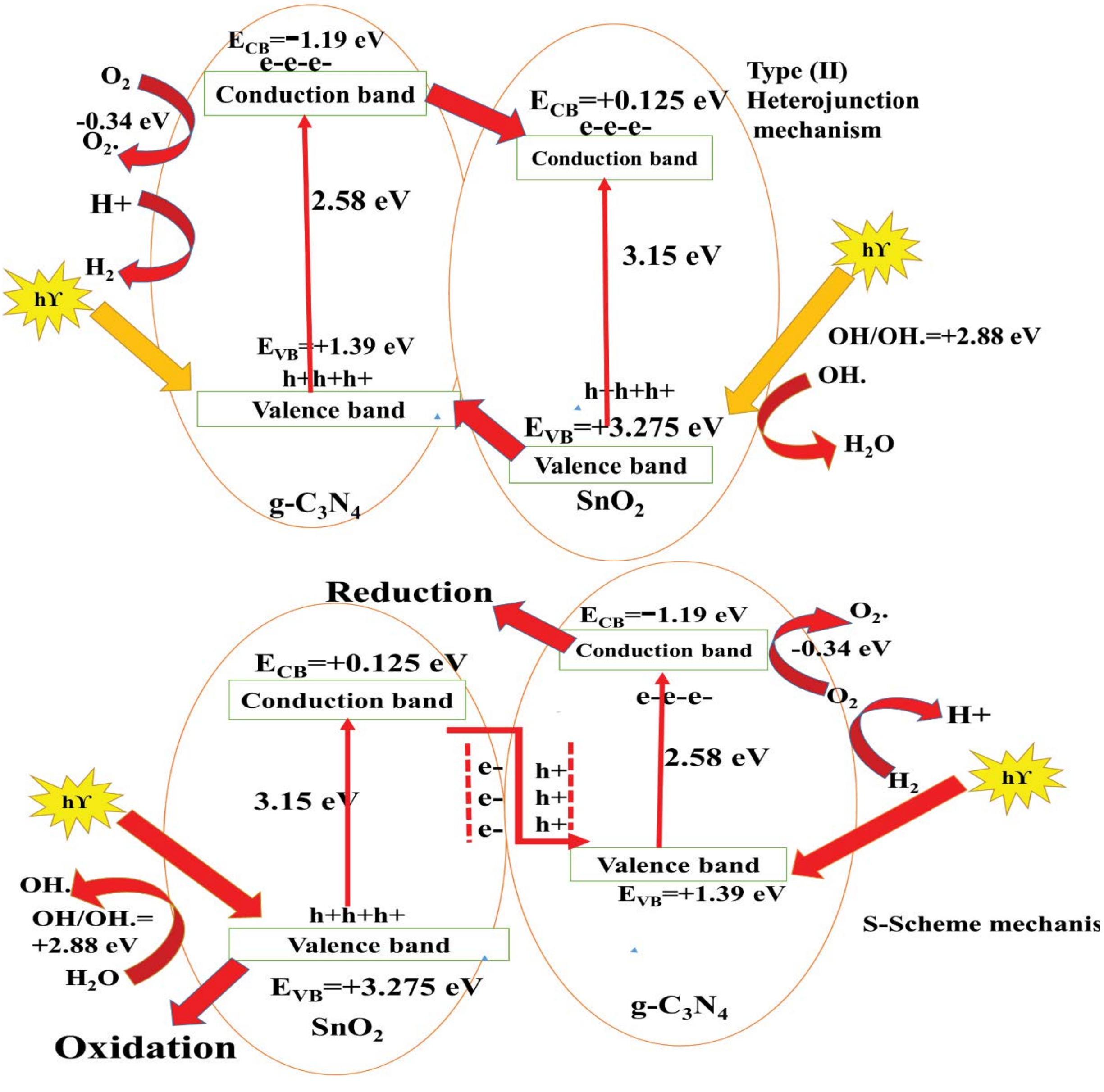

Fig. 7. Scheme for charge migration between SnO_2 and g-C_3N_4 through direct S-scheme and type (II) heterojunction.

holes and SnO_2 negative electrons are sacrificed. The VB positive holes of SnO_2 with potential 3.275 eV are readily generate hydroxyl radicals (OH^-/OH.) and g-C_3N_4 conduction band electrons with potential –1.10 eV reduces H^+ and generating hydrogen gas (Fig. 7). The proposed mechanism for step S-scheme mechanism require electron transportation from VB to CB of both g-C_3N_4 and SnO_2 energy levels followed by recombination of holes and electrons with low redox potential leaving the charge carriers in the higher valence and conduction bands maintained with strong redox potential (Fig. 7). The charge transportation processes is accompanied by generation of a built-in electric field at the g-C_3N_4/SnO_2 interface, S-scheme interfacial charge transportation require photogenerated electrons transfer from the CB of SnO_2 toward the VB of g-C_3N_4 upon exposure of light. The holes in g-C_3N_4 and the electrons in SnO_2 with weak redox efficiency were sacrificed, and the electrons in g-C_3N_4 and the holes in SnO_2 with enhanced redox ability are preserved and were spatially separated, which together modulate the charge potentials and dynamics to suit the requirement of dual functionality for photocatalytic reduction and oxidation processes. The holes in the VB of SnO_2 activated H_2O for the production of $^{\bullet}OH$ results in oxidation of fluorescein dye. The electron-initiated reactions transfer O_2 by the CB electrons of g-C_3N_4 to produce $^{\bullet}O_2$–.

3.5. Comparative studies with previous literature

Compared our research results with those reported by other authors following the photocatalytic degradation of organic dye and photocatalytic hydrogen production

Table 1
Comparative study of photodegradation of various organic pollutants over g-C_3N_4/SnO_2

Photocatalyst	Preparation	Photodegradation of organic pollutant (%)	Reference
g-C_3N_4/SnO_2	Sonochemical	95% of fluorescein dye	Our research
g-C_3N_4/SnO_2	Precipitation method	94% of methyl orange dye	[39]
g-C_3N_4/SnO_2	Hydrothermal method	85% of methylene blue dye	[46]
g-C_3N_4/SnO_2	Freeze dry	88% of rhodamine B dye	[47]
g-C_3N_4/SnO_2	Hydrothermal method	90% of indomethacin	[48]
g-C_3N_4/SnO_2	Mechanical method	92% of rhodamine B dye	[51]
g-C_3N_4/SnO_2	Wet chemical method	90% of rhodamine B dye	[49]
g-C_3N_4/SnO_2	Physical mixing method	90% of methyl orange dye	[50]

Table 2
Comparative study of photocatalytic hydrogen evolution over g-C_3N_4/SnO_2

Photocatalyst	Preparation method	Amount of hydrogen gas evolved (mmol/h g)	References
g-C_3N_4/SnO_2	Sonochemical	6.8	Our research
Pt/g-C_3N_4/SnO_2	Hydrothermal	1.06	[52]
0D/2D SnO_2/g-C_3N_4	Step polymerization	1.38	[53]

Table 3
Nomenclature of the as-synthesized samples

Sample	Nomenclature
Tin oxide	SnO_2
Graphitic carbon nitride	CN
Tin oxide + 5 wt.% graphitic carbon nitride	SnCN5
Tin oxide + 10 wt.% graphitic carbon nitride	SnCN10
Tin oxide + 15 wt.% graphitic carbon nitride	SnCN15
Tin oxide + 20 wt.% graphitic carbon nitride	SnCN20

Table 4
Nomenclature of the as-synthesized samples

Sample	Nomenclature
Tin oxide	SnO_2
Graphitic carbon nitride	CN
Tin oxide + 5wt %Graphitic carbon nitride	SnCN5
Tin oxide + 10wt %Graphitic carbon nitride	SnCN10
Tin oxide + 15wt %Graphitic carbon nitride	SnCN15
Tin oxide + 20wt %Graphitic carbon nitride	SnCN20

[39–47], our heterojunction with composition 10% g-C_3N_4 and 90% SnO_2 exhibit an exceptional reactivity in decompose 90% of fluorescein dye and produce hydrogen gas with rate 6.77 mmol h^{-1} g^{-1} (Tables 2 and 3). The nomenclature for the as-synthesized samples is illustrated in Table 4.

4. Conclusions

A synergetic effect between g-C_3N_4 sheets and SnO_2 nanoparticles generate a successful step- S-scheme heterojunction with exceptional reactivity in decompose fluorescein dye and produce a considerable amount of hydrogen gas. The adjusted band gap energy levels of SnO_2 and g-C_3N_4 facilitate the separation of the photo-generated carriers and boosting the efficiency of interfacial charge transfer. The photocatalytic nanocomposites were generated by ultrasonic route with 150 W intensity. Heterojunction containing 10 wt.% of g-C_3N_4 exhibits the optimum reactivity in photocatalytic degradation of fluorescein dye and production of hydrogen gas. PL and scavengers trapping experiments reveals that the charge migration proceeds adopting step S-scheme mechanism. Thoroughly, step-S scheme mechanism, the holes and electrons with low redox potential are scarified. On the other hand, the holes and electrons with high redox potential are maintained with strong redox power for fluorescein dye degradation and strong reducing power for production of hydrogen gas. The durability of the optimal specimen SnCN10 exhibit a better stability after six consecutive cycles of either photocatalytic decomposition of fluorescein dye and hydrogen gas evolution.

Acknowledgment

The authors extend their appreciation to the Deanship of Scientific Research at King Khalid University for funding this work through the Research Group Program under grant number RGP.1/286/42.

References

[1] M.A. Ahmed, N. Al-Zaqri, A. Alsalme, A.H. Glal, M. Esa, Rapid photocatalytic degradation of RhB dye and photocatalytic hydrogen production on novel curcumin/SnO_2 nanocomposites through direct Z-scheme mechanism, J. Mater. Sci. - Mater. Electron., 31 (2020) 19188—19203

[2] M.A. Ahmed, A. Fahmy, M.G. Abuzaid, E.M. Hashem, Fabrication of novel $AgIO_4$/SnO_2 heterojunction for photocatalytic hydrogen production through direct Z-scheme

mechanism, J. Photochem. Photobiol., A, 400 (2020) 112660, doi: 10.1016/j.jphotochem.2020.112660.

[3] Z.M. Abou-Gamra, M.A. Ahmed, M.A. Hamza, Investigation of commercial $PbCrO_4/TiO_2$ for photodegradation of rhodamine B in aqueous solution by visible light, Nanotechnol. Environ. Eng., 2 (2017) 12, doi: 10.1007/s41204-017-0024-9.

[4] A.H. Galal, M.G. Elmahgary, M.A. Ahmed, Construction of novel $AgIO_4$/ZnO/graphene direct Z-scheme heterojunctions for exceptional photocatalytic hydrogen gas production, Nanotechnol. Environ. Eng., 6 (2020) 5, doi: 10.1007/s41204-020-00096-8.

[5] X. Liu, Y.X. Zhao, X.F. Yang, Q.Q. Liu, X.H. Yu, Y.Y. Li, H. Tang, T.R. Zhang, Porous Ni_5P_4 as a promising cocatalyst for boosting the photocatalytic hydrogen evolution reaction performance, Appl. Catal., B, 275 (2020) 119144, doi: 10.1016/j.apcatb.2020.119144.

[6] C. Prasad, H. Tang, Q.Q. Liu, I. Bahadur, S. Karlapudi, Y.J. Jiang, A latest overview on photocatalytic application of g-C_3N_4 based nanostructured materials for hydrogen production, Int. J. Hydrogen Energy, 45 (2020) 337–379.

[7] M.A. Ahmed, Z.M. Abou-Gamra, M.A. ALshakhanbeh, H. Medien, Control synthesis of metallic gold nanoparticles homogeneously distributed on hexagonal ZnO nanoparticles for photocatalytic degradation of methylene blue dye, Environ. Nanotechnol. Monit. Manage., 12 (2019) 100217, doi: 10.1016/j.enmm.2019.100217.

[8] H.N. Wang, Z.Q. Lv, J. Zhang, Y. Xiang, S.F. Lu, The effect of functional groups on the electrocatalytic activity of carbon nanotubes with different wall numbers toward carbohydrazide oxidation reaction, Chem.-An Asian J., 15 (2020) 3456–3461.

[9] F.A. Fouad, M.A. Ahmed, M.S. Antonious, M.F. Abdel-Messih, Synthesis of an efficient, stable and recyclable $AgVO_3$/ZnO nanocomposites with mixed crystalline phases for photocatalytic removal of rhodamine B dye, J. Mater. Sci. - Mater. Electron., 31 (2020) 12355–12371.

[10] H.S.M. Abd-Rabboh, M. Benaissa, M.A. Ahmed, K.F. Fawy, M.S. Hamdy, Facile synthesis of spherical Au/TiO_2 nanoparticles by sol–gel method using Tween 80 for photocatalytic decolourization of Malachite Green dye, Mater. Res. Express, 6 (2019) 025028.

[11] W.H. Niu, K. Marcus, L. Zhou, Z. Li, L. Shi, K. Liang, Y. Yang, Enhancing electron transfer and electrocatalytic activity on crystalline carbon-conjugated g-C_3N_4, ACS Catal., 8 (2018) 1926–1931.

[12] H.J. Yu, L. Shang, T. Bian, R. Shi, G.I.N. Waterhouse, Y.F. Zhao, C. Zhou, L.-Z. Wu, C.-H. Tung, T.R. Zhang, Nitrogen-doped porous carbon nanosheets templated from g-C_3N_4 as metal-free electrocatalysts for efficient oxygen reduction reaction, Adv. Mater., 28 (2016) 5080–5086.

[13] S.B. Tian, Z.Y. Wang, W.B. Gong, W.X. Chen, Q.C. Feng, Q. Xu, C. Chen, C. Chen, Q. Peng, L. Gu, H.J. Zhao, P. Hu, D.S. Wang, Y.D. Li, Temperature-controlled selectivity of hydrogenation and hydrodeoxygenation in the conversion of biomass molecule by the Ru1/mpg-C_3N_4 catalyst, J. Am. Chem. Soc., 140 (2018) 11161–11164.

[14] H. Liu, X.Y. Liu, W.W. Yang, M.Q. Shen, S. Geng, C. Yu, B. Shen, Y.S. Yu, Photocatalytic dehydrogenation of formic acid promoted by superior PdAg@g-C_3N_4 Mott-Schottky heterojunction, J. Mater. Chem. A, 7 (2019) 2022–2026.

[15] C.M. Li, Y.H. Du, D.P. Wang, S.M. Yin, W.G. Tu, Z. Chen, M. Kraft, G. Chen, R. Xu, Unique P-Co-N surface bonding states constructed on g-C_3N_4 nanosheets for drastically enhanced photocatalytic activity of H_2 evolution, Adv. Funct. Mater., 27 (2017) 1604328, doi: 10.1002/adfm.201604328.

[16] C.M. Li, Y. Xu, W.G. Tu, G. Chen, R. Xu, Metal-free photocatalysts for various applications in energy conversion and environmental purification, Green Chem., 19 (2017) 882–899.

[17] M. Mousavi, A. Habibi-Yangjeh, S.R. Pouran, Review on magnetically separable graphitic carbon nitride-based nanocomposites as promising visible-light-driven photocatalysts, J. Mater. Sci. - Mater. Electron., 29 (2018) 1719–1747.

[18] N. Al-Zaqri, A. Alsalme, M.A. Ahmed, A.H. Galal, Construction of novel direct Z-scheme $AgIO_4$-g-C_3N_4 heterojunction for photocatalytic hydrogen production and photodegradation of fluorescein dye, Diamond Relat. Mater., 109 (2020) 108071, doi: 10.1016/j.diamond.2020.108071.

[19] H.S.M. Abd-Rabboh, A.H. Galal, R.A. Aziz, M.A. Ahmed, A novel $BiVO_3/SnO_2$ step S-scheme nano-heterojunction for an enhanced visible light photocatalytic degradation of amaranth dye and hydrogen production, RSC Adv., 11 (2021) 29507–29518.

[20] K.N. Van, H.T. Huu, V.N.N. Thi, T.L.L. Thi, D.H. Truong, T.T. Truong, N.N. Dao, V. Vo, D.L. Tran, Y. Vasseghian, Facile construction of S-scheme SnO_2/g-C_3N_4 photocatalyst for improved photoactivity, Chemosphere, 289 (2022) 133120, doi: 10.1016/j.chemosphere.2021.133120.

[21] A. Zada, M. Humayun, F. Raziq, X.L. Zhang, Y. Qu, L.L. Bai, C.L. Qin, L.Q. Jing, H.G. Fu, Exceptional visible-light-driven cocatalyst-free photocatalytic activity of g-C_3N_4 by well-designed nanocomposites with plasmonic Au and SnO_2, Adv. Energy Mater., 6 (2016) 1601190, doi: 10.1002/aenm.201601190.

[22] R. Yin, Q.Z. Luo, D.S. Wang, H.T. Sun, Y.Y. Li, X.Y. Li, J. An, SnO_2/g-C_3N_4 photocatalyst with enhanced visible-light photocatalytic activity, J. Mater. Sci., 49 (2014) 6067–6073.

[23] Y.P. Zang, L.P. Li, X.G. Li, R. Lin, G.S. Li, Synergistic collaboration of g-C_3N_4/SnO_2 composites for enhanced visible-light photocatalytic activity, Chem. Eng. J., 246 (2014) 277–286.

[24] A. Zada, M. Khan, M.N. Qureshi, S.-y. Liu, R.D. Wang, Accelerating photocatalytic hydrogen production and pollutant degradation by functionalizing g-C_3N_4 with SnO_2, Front. Chem., 7 (2019) 941, doi: 10.3389/fchem.2019.00941.

[25] K.X. Zhu, Y. Lv, J. Liu, W.J. Wang, C.P. Wang, S.M. Li, P. Wang, M. Zhang, A. Meng, Z.J. Li, Facile fabrication of g-C_3N_4/SnO_2 composites and ball milling treatment for enhanced photocatalytic performance, J. Alloys Compd., 802 (2019) 13–18.

[26] H.S.M. Abd-Rabboh, M. Benaissa, M.S. Hamdy, M.A. Ahmed, M. Glal, Synthesis of an efficient, and recyclable mesoporous $BiVO_4/TiO_2$ direct Z-scheme heterojunction by sonochemical route for photocatalytic hydrogen production and photodegradation of rhodamine B dye in the visible region, Opt. Mater., 114 (2021) 110761, doi: 10.1016/j.optmat.2020.110761.

[27] R. Abdel-Aziz, M.A. Ahmed, M.F. Abdel-Messih, A novel UV and visible light driven photocatalyst $AgIO_4$/ZnO nanoparticles with highly enhanced photocatalytic performance for removal of rhodamine B and indigo carmine dye, J. Photochem. Photobiol., A, 389 (2020) 112245, doi: 10.1016/j.jphotochem.2019.112245.

[28] M.A. Ahmed, M.F. Abdel-Messih, E.H. Ismail, Facile synthesis of novel microporous CdSe/SiO_2 nanocomposites selective for removal of methylene blue dye by tandem adsorption and photocatalytic process, J. Mater. Sci. - Mater. Electron., 30 (2019) 17527–17539.

[29] M.F. Abdel Messih, A.E. Shalan, M.F. Sanad, M.A. Ahmed, Facile approach to prepare ZnO@SiO_2 nanomaterials for photocatalytic degradation of some organic pollutant models, J. Mater. Sci. - Mater. Electron., 30 (2019) 1491–1499.

[30] Q.L. Xu, L.Y. Zhang, B. Cheng, J.J. Fan, J.G. Yu, S-scheme heterojunction photocatalyst, Chem, 6 (2020) 1543–1559.

[31] S. Wageh, A.A. Al-Ghamdi, R. Jafer, X. Li, P. Zhang, A new heterojunction in photocatalysis: S-scheme heterojunction, Chin. J. Catal., 42 (2021) 667–669.

[32] A. Alsalme, A.H. Galal, E.F. El-Sherbeny, A. Soltan, M.F. Abdel-Messih, M.A. Ahmed, Fabrication of S-scheme TiO_2/g-C_3N_4 nanocomposites for generation of hydrogen gas and removal of fluorescein dye, Diamond Relat. Mater., 122 (2022) 108819, doi: 10.1016/j.diamond.2022.108819.

[33] A.Y. Meng, B. Cheng, H.Y. Tan, J.J. Fan, C.L. Su, J.G. Yu, TiO_2/polydopamine S-scheme heterojunction photocatalyst with enhanced CO_2-reduction selectivity, Appl. Catal., B, 289 (2021) 120039, doi: 10.1016/j.apcatb.2021.120039.

[34] Y.X. Xiao, Z. Ji, C. Zou, Y.Q. Xu, R. Wang, J. Wu, G.L. Liu, P. He, Q. Wang, T. Jia, Construction of CeO_2/BiOI S-scheme heterojunction for photocatalytic removal of elemental mercury, Appl. Surf. Sci., 556 (2021) 149767, doi: 10.1016/j.apsusc.2021.149767.

[35] H.N. Ge, F.Y. Xu, B. Cheng, J.G. Yu, W.K. Ho, S-scheme heterojunction TiO_2/CdS Nanocomposites fibers as H_2-production photocatalyst, ChemCatChem, 11 (2019) 6301–6309.

[36] Q.Q. Li, W.L. Zhao, Z.C. Zhai, K.X. Ren, T.Y. Wang, H. Guan, H.F. Shi, 2D/2D Bi_2MoO_6/g-C_3N_4 S-scheme heterojunction photocatalyst with enhanced visible-light activity by Au loading, J. Mater. Sci. Technol., 56 (2020) 216–226.

[37] S. Jiang, J. Cao, M. Guo, D.D. Cao, X.M. Jia, H.L. Lin, S.F. Chen, Novel S-scheme WO_3/RP composite with outstanding overall water splitting activity for H_2 and O_2 evolution under visible light, Appl. Surf. Sci., 558 (2021) 149882, doi: 10.1016/j.apsusc.2021.149882.

[38] X.F. Zhang, Y. Zhang, X.B. Jia, N. Zhang, R. Xia, X.J. Zhang, Z.W. Wang, M.Q. Yu, In situ fabrication of a novel S-scheme heterojunction photocatalyts Bi_2O_3/P-C_3N_4 to enhance levofloxacin removal from water, Sep. Purif. Technol., 268 (2021) 118691, doi: 10.1016/j.seppur.2021.118691.

[39] Q.Q. Liu, X.D. He, J.J. Peng, X.H. Yu, H. Tang, J. Zhang, Hot-electron-assisted S-scheme heterojunction of tungsten oxide/graphitic carbon nitride for broad-spectrum photocatalytic H_2 generation, Chin. J. Catal., 42 (2021) 1478–1487.

[40] K. Zhang, D.Q. Li, Q.Y. Tian, H.Y. Cao, F. Orudzhev, I.A. Zvereva, J.K. Xu, C.Y. Wang, Recyclable 0D/2D $ZnFe_2O_4$/$Bi_5FeTi_3O_{15}$ S-scheme heterojunction with bismuth decoration for enhanced visible-light-driven tetracycline photodegradation, Ceram. Int., 47 (2021) 17109–17119.

[41] S.S. Wu, X. Yu, J.L. Zhang, Y.M. Zhang, Y. Zhu, M.S. Zhu, Construction of BiOCl/$CuBi_2O_4$ S-scheme heterojunction with oxygen vacancy for enhanced photocatalytic diclofenac degradation and nitric oxide removal, Chem. Eng. J., 411 (2021) 128555, doi: 10.1016/j.cej.2021.128555.

[42] Q. Wang, Y.M. Lin, P.Y. Li, M.T. Ma, V. Maheskumar, Z.Y. Jiang, R.Q. Zhang, An efficient Z-scheme (Cr, B) codoped g-C_3N_4/$BiVO_4$ photocatalyst for water splitting: a hybrid DFT study, Int. J. Hydrogen Energy, 46 (2021) 247–261.

[43] J. Singh, P. Kumari, S. Basu, Degradation of toxic industrial dyes using SnO_2/g-C_3N_4 nanocomposites: role of mass ratio on photocatalytic activity, J. Photochem. Photobiol., A, 371 (2019) 136–143.

[44] V.V. Pham, D.-Q. Mai, D.-P. Bui, T.V. Man, B.C. Zhu, L.Y. Zhang, J. Sangkaworn, J. Tantirungrotechai, V. Reutrakul, T.M. Cao, Emerging 2D/0D g-C_3N_4/SnO_2 S-scheme photocatalyst: new generation architectural structure of heterojunctions toward visible-light-driven NO degradation, Environ. Pollut., 286 (2021) 117510, doi: 10.1016/j.envpol.2021.117510.

[45] B. Babu, M.Y. Cho, C. Byon, J. Shim, Sunlight-driven photocatalytic activity of SnO_2 QDs-g-C_3N_4 nanolayers, Mater. Lett., 212 (2018) 327–331.

[46] A. Mohammad, M.E. Khan, M.R. Karim, M.H. Cho, Synergistically effective and highly visible light responsive SnO_2-g-C_3N_4 nanostructures for improved photocatalytic and photoelectrochemical performance, Appl. Surf. Sci., 495 (2019) 143432, doi: 10.1016/j.apsusc.2019.07.174.

[47] P. Prausa, L. Svoboda, R. Dvorský, M. Reli, Nanocomposites of SnO_2 and g-C_3N_4: preparation, characterization and photocatalysis under visible LED irradiation, Ceram. Int., 44 (2018) 3837–3846.

[48] D.G. Li, J.X. Huang, R.B. Li, P. Chen, D. Chen, M.X. Cai, H.J. Liu, Y.P. Feng, W.Y. Lv, G.G. Liu, Synthesis of a carbon dots modified g-C_3N_4/SnO_2 Z-scheme photocatalyst with superior photocatalytic activity for PPCPs degradation under visible light irradiation, J. Hazard. Mater., 401 (2021) 123257, doi: 10.1016/j.jhazmat.2020.123257.

[49] J. Singh, P. Kumari, S. Basu, Degradation of toxic industrial dyes using SnO_2/g-C_3N_4 nanocomposites: role of mass ratio on photocatalytic activity, J. Photochem. Photobiol., A, 371 (2018) 136–143.

[50] Y.P. Zang, L.P. Li, X.G. Li, R. Lin, G.S. Li, Synergistic collaboration of g-C_3N_4/SnO_2 composites for enhanced visible-light photocatalytic activity, Chem. Eng. J., 246 (2014) 277–286.

[51] Y.M. He, L.H. Zhang, M.H. Fan, X.X. Wang, M.L. Walbridge, Q.Y. Nong, Y. Wu, L.H. Zhao, Z-scheme SnO_{2-x}/g-C_3N_4 composite as an efficient photocatalyst for dye degradation and photocatalytic CO_2 reduction, Sol. Energy Mater. Sol. Cells, 137 (2015) 175–184.

[52] X.K. Wang, M.R. Xue, X.Q. Li, L.X. Qin, S.-Z. Kang, Boosting the photocatalytic H_2 production performance and stability of C_3N_4 nanosheets via the synergistic effect between SnO_2 nanoparticles and Pt nanoclusters, Inorg. Chem. Commun., 133 (2021) 108976, doi: 10.1016/j.inoche.2021.108976.

[53] H.H. Wu, S.Y. Yu, Y. Wang, J. Han, L. Wang, N. Song, H.J. Dong, C.M. Li, A facile one-step strategy to construct 0D/2D SnO_2/g-C_3N_4 heterojunction photocatalyst for high-efficiency hydrogen production performance from water splitting, Int. J. Hydrogen Energy, 45 (2020) 30142–30152.